Nano Today 48 (2023) 101691

Contents lists available at ScienceDirect

Nano Today

journal homepage: www.elsevier.com/locate/nanotoday

Semiconducting polymer nanomanipulators for thermal sensitization and metastasis-inhibited synergistic cancer therapy

Min Wu, Rui Qu, Haoze Li, Linrong Chen, Xiaoke Zhang, Yang Yuan, Weizhi Chen, Xiqun Jiang *, Xu Zhen *

MOE Key Laboratory of High Performance Polymer Materials and Technology, and Department of Polymer Science & Engineering, College of Chemistry & Chemical Engineering, Nanjing University, Nanjing 210023, PR China

ARTICLE INFO

Article history:
Received 14 August 2022
Received in revised form 24 October 2022
Accepted 13 November 2022
Available online xxxx

Keywords:
Cancer therapy
Photo-manupulation
Thermal sensitization
Metastasis inhibition
Semiconducting polymer nanoparticles

ABSTRACT

Manipulation of intracellular protein expression is a promising cancer therapeutic approach; however, traditional strategies relying on nonspecific molecular drugs often suffer from limited therapeutic benefits and off-target adverse events. Here, we report a semiconducting polymer nanomanipulator (SPNm) that can photothermally manipulate intracellular protein expression to synergize with its own function of second near-infrared (NIR-II) photothermal therapy (PTT) for thermal sensitization and metastasis-inhibited cancer therapy. SPNm comprises an NIR-II absorbing semiconducting polymer core as a photothermal transduction agent and a lysine-specific histone demethylase 3 A (KDM3A) inhibitor as a downstream effector protein expression manipulator, which are encapsulated into a thermo-responsive lipid shell. Upon 1064 nm laser irradiation, SPNm mediates the photothermal effect to melt the lipid shell for on-demand release of the KDM3A inhibitor to inhibit the demethylation function of KDM3A to upregulate the level of di-methylation of histone H3 lysine 9 (H3K9me2), and in turn simultaneously downregulate the expression of heat-shock protein 90 (HSP90) and cancer cell metastasis-related proteins, consequently inhibiting the thermotolerance response and metastasis of cancer cells. Thus, a single treatment of SPNm-mediated two-step NIR-II phototherapy achieves efficient tumor growth suppression at an unprecedented photothermal ablation depth (1 cm) and lung metastasis inhibition. Therefore, this study provides a promising thermal-controlled strategy to synergize phototherapeutics with protein expression manipulation for enhanced cancer treatment.

Introduction

Manipulation of intracellular protein expression provides a novel therapeutic strategy for cancer therapy [1–3]. Delivery of molecular drugs into cancer cells to manipulate oncogenic or antioncogenic protein expression has been considered a promising cancer therapeutic approach [4,5]. For example, hypoxia-inducible transcription factor (HIF)− 1α inhibitors, such as KC7F2 or YC-1, inhibit HIF-1α expression levels by promoting HIF-1α degradation and downregulating HIF-1α protein synthesis to achieve an effective antitumor effect [6,7]. Kevetrin, a small molecular activator of the tumor suppressor protein p53, activates p53, which in turn upregulates the expression of p21 to induce cell cycle arrest and apoptosis [8]. However, the nonspecific distribution of these protein expression manipulators in normal tissues generally results in limited therapeutic benefits and adverse events [9]. To tackle these issues, nanoagents that release molecular drugs in response to endogenous tumor microenvironment related biomarkers (e.g. acidic pH, reactive oxygen species, enzymes, and hypoxia) have been developed to selectively manipulate protein expression for optimized cancer therapy [10–13]. However, such strategies merely rely on the concentration difference of biomarkers in normal and pathological environments, which inevitably limits their release efficiency. Thus, alternative strategies to precisely control drug release and achieve on-demand manipulation of intracellular protein expression are highly desired.

Exogenous stimuli, including light [14], ultrasound [15,16], X-ray [17], and electromagnetism [18] can provide remote control of the pharmacological action of molecular drugs regardless of pathological characteristics. Among them, light holds great potential for precisely controlling drug activity due to its noninvasiveness, high spatiotemporal controllability and simple operation [19–23]. In particular,

* Corresponding author.
E-mail addresses: jiangx@nju.edu.cn (X. Jiang), zhenxu@nju.edu.cn (X. Zhen).

https://doi.org/10.1016/j.nantod.2022.101691
1748-0132/

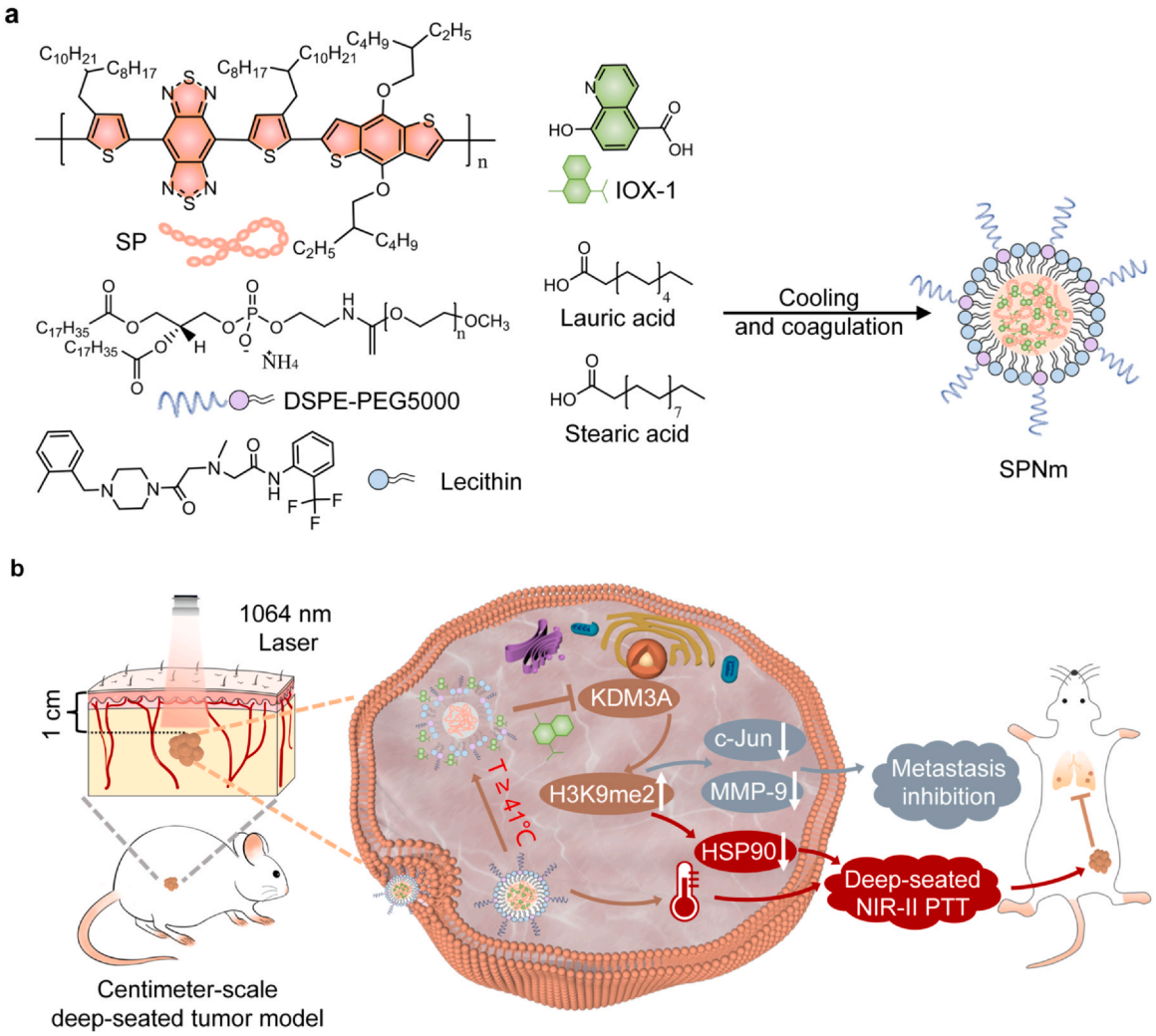

Fig. 1. SPNm-mediated thermal sensitization and metastasis-inhibited synergistic cancer therapy. a) Chemical structures of SP, lecithin, DSPE-PEG5000, IOX-1, lauric acid, and stearic acid, and the preparation process of SPNm. b) Schematic illustration of the NIR-II photo-manipulation mechanism of SPNm for thermal sensitization and metastasis-inhibited synergistic cancer therapy.

near-infrared (NIR) light has been utilized for photoactivation of enzymatic activity [24], photoregulation of gene editing [25], and controlled release of small molecular drugs [26]. However, most existing light-controlled nanoagents rely on the first NIR window (NIR-I, 650–900 nm) light with limited tissue penetration depth [27]. In contrast, second NIR window (NIR-II, 900–1700 nm) light is attracting more attention due to the reduced tissue attenuation and reabsorption relative to the NIR-I window, resulting in a greater tissue penetration depth exceeding 1 cm in biological tissues and a higher maximum permission energy (MPE) (1 W cm^{-2} for 1064 nm while 0.3 W cm^{-2} for 808 nm) for skin irradiation [28]. NIR-II light-responsive nanoagents, including gold nanomaterials [29,30], copper sulfide nanomaterials [31], two-dimensional materials [32] and small molecular dyes [33–36], have been extensively applied for phototherapy and optical imaging. However, photo-manipulation of intracellular protein expression by NIR-II light-responsive nanoagents has yet to be expoited.

We herein report a semiconducting polymer nanomanipulator (SPNm) with NIR-II photothermal function to precisely manipulate the expression of a series of intracellular proteins for thermal sensitization and metastasis-inhibited synergistic cancer therapy. SPNm comprises a highly NIR-II absorbing semiconducting polymer core and a protein expression manipulator encapsulated into a thermo-responsive lipid shell (Fig. 1a). Semiconducting polymer nanoparticles (SPNs) composed of highly π-conjugated backbones with tunable photophysical properties, structural diversity, and good biocompatibility have been widely applied for ultrasensitive disease diagnostics and therapeutic interventions [37–44]. Lysine-specific histone demethylase 3 A (KDM3A) plays a key role in promoting gene expression by removing the mono- and di-methylation of histone H3 lysine 9 and is overexpressed in multiple cancer types, including 4T1 murine mammary carcinoma cells, MCF-7 human breast cancer cells and H23 human lung cancer cells [45,46]. 5-Carboxy-8-hydroxyquinoline (IOX-1) [47], an inhibitor of the KDM3A, was selected as the manipulator molecule. Lecithin, lauric acid (LA), stearic acid (SA), and 1,2-distearoyl-sn-glycero-3-phosphoethanolamine-poly (ethylene glycol5000) (DSPE-PEG5000) were utilized to fabricate the thermo-responsive lipid shell [48,49]. After systemic administration, SPNm can preferentially accumulate and be retained in the tumor site through the enhanced permeation and retention (EPR) effect for a long time. Upon photoirradiation at 1064 nm, SPNm exerts efficient photothermal conversion to increase the local temperature, which melts the thermo-responsive lipid shells for the release of IOX-1 at the tumor site. The released KDM3A inhibitor IOX-1 inhibits the demethylation function of KDM3A to upregulate the level of di-methylation of histone H3 lysine 9 (H3K9me2) in cancer cells, which in turn leads to the down-regulation of a series of KDM3A downstream effector proteins

including heat shock protein 90 (HSP90) and cancer cell metastasis-related proteins c-Jun and matrix metalloproteinase-9 (MMP-9), leading to the enhanced sensitivity of cancer cells to thermal-induced cell death and metastasis inhibition [50,51]. As such, centimeter-scale deep-seated tumors and lung metastasis can be simultaneously suppressed by synergistic integration of NIR-II photothermal therapy (PTT) and photo-manipulation protein expression therapy (Fig. 1b).

Results

Synthesis and characterization

The NIR-II absorbing semiconducting polymer (SP) was obtained via palladium-catalyzed Stille polycondensation of benzobisthiadiazole and (4,8-bis((2-ethylhexyl)oxy) benzo[1,2-b:4,5-b′]dithiophene-2,6-diyl)bis(trimethylstannane) (Fig. S1). Proton nuclear magnetic resonance (^{1}H NMR) confirmed the successful synthesis of SP (Fig. S2). The number average molecular weight of the obtained SP was determined to be ~6000 Da by gel permeation chromatography (Fig. S3). The obtained SP showed a strong absorption in the NIR-II window (Fig. S4). Water-soluble SPNm was obtained through the nanoprecipitation method in the presence of SP, IOX-1, DSPE-PEG5000, lecithin, LA, and SA with a feeding weight ratio of 1.25:1:5:15:10:2. The eutectic mixture of LA and SA was chosen as the gating material to prepare a thermo-responsive lipid shell. SP and IOX-1 were encapsulated into thermo-responsive lipid shell through hydrophobic and π-π stacking interactions [14]. The encapsulation efficiency was calculated to be 46 % for IOX-1. For comparison, the control counterpart (termed SPNc) was also constructed via a similar method except for the addition of IOX-1.

The physical and photothermal properties of SPNm were investigated and compared with those of SPNc. Dynamic light scattering (DLS) analysis showed similar hydrodynamic sizes of SPNm (69 nm) and SPNc (68 nm) (Fig. 2a). The spherical morphology with dimension homogeneousness for both SPNm and SPNc was further confirmed by transmission electron microscopy (TEM) (Fig. 2a, inset). The hydrodynamic sizes of both nanoparticles remained almost unchanged during storage in aqueous solution, 1 × phosphate buffer solution (PBS) and PBS containing 10 % serum for 15 days (Fig. S5), indicating their excellent colloidal stability. Both SPNm and SPNc exhibited similar broad absorption in the range of 950–1100 nm with maxima at 995 nm (Fig. 2b). Upon continuous photoirradiation at 1064 nm (1 W cm^{-2}), both nanoparticles induced a significant solution temperature rise and similarly reached a plateau (~80 °C) at t = 6 min (Fig. 2c). Such results verified the negligible influence on the optical and photothermal properties of SPNm after encapsulation of IOX-1. The photothermal conversion efficiencies of both SPNm and SPNc were calculated to be ~80 % (Fig. S6). The maximum temperature of both nanoparticles remained almost unchanged for at least 6 cycles of heating and natural cooling during storage (Fig. S7), which indicated their good photothermal stability.

The photothermally triggered release of IOX-1 from SPNm was tested. The eutectic mixture, formulated from LA (melting point = 45 ~ 48 °C) and SA (melting point = 70 ~ 73 °C) at a mass ratio of 5:1 showed a sharp melting point at 41 °C using differential scanning calorimetry (DSC) analysis (Fig. 2d), which is suitable for the thermo-responsive on-demand release of IOX-1 in the physiological setting. To further confirm the melting temperature of SPNm, the lipophilic membrane dye DiO (4 % w/w), was doped into nanoparticles during the nanoprecipitation process (Fig. S8). The DiO-doped SPN (termed SPND) showed a new characteristic absorption peak at 488 nm, and a new fluorescence emission peak at 501 nm in comparison with SPNc (Fig. S9), verifying the successful doping of DiO into nanoparticles. With the solution temperature rising from 37° to 45°C, the fluorescence of SPND at 501 nm gradually decreased due to the environment-sensitive fluorescence behavior of DiO [52], implying the release of DiO from SPND (Fig. 2e and Fig. S10). Furthermore, sharp fluorescence changes between 39 and 42 °C were observed, indicating that the phase-transition temperature of SPNm was approximately 41 °C, which was consistent with the DSC results. Therefore, upon 1064 nm laser irradiation of SPNm solution for 10 min (the maximum temperature was maintained at approximately 43 °C by controlling the laser power), an elution peak at 20.2 min corresponding to IOX-1 was observed through high performance liquid chromatography (HPLC) (Fig. 2f). In contrast, no obvious release of IOX-1 from SPNm could be observed without laser irradiation, even after a long-term period of storage (Fig. 2f. and Fig. S11). The molecular weight of released IOX-1 was further validated by high resolution electrospray ionization mass spectrometry (HR-ESI-MS) (Fig. S12), indicating the good thermostability of IOX-1 upon NIR-II laser irradiation. Furthermore, the release ratio of IOX-1 from SPNm was calculated to be 62 % upon laser irradiation for 10 min. The correlated mechanism of the photothermally controlled release was proposed as follows: upon laser irradiation, the increased temperature of SPNm melted the lipid shell of thermo-responsive nanoparticles with a phase-transition temperature of approximately 41 °C, resulting in the controlled release of IOX-1.

To evaluate the centimeter-scale deep tissue photothermal heating capabilities of both SPNm and SPNc, the nanoparticle solution was filled in an Eppendorf tube covered by a piece of chicken breast tissue with 1 cm thickness and then irradiated at 1064 nm (1 W cm^{-2}) for 10 min (Fig. 2g). The temperature increases of both SPNm and SPNc solutions reached 19.5 °C with a tissue depth of 1 cm under 1064 nm laser irradiation (Figs. 2h and 2i). Considering the average body temperature (≈32–35 °C during anesthesia) and the threshold temperatures for photothermally induced IOX-1 release (41 °C) and cancer cell necrosis and apoptosis (43–46 °C) [53,54], such a temperature increment of SPNm solution was sufficient to induce the release of IOX-1 and thermal ablation of cancer cells in living mice.

In Vitro SPNm-mediated synergistic cancer therapy and therapeutic mechanism

The biocompatibility of SPNm and SPNc was first investigated using normal cells (MCF-10A) and breast cancer cells (4T1). After MCF-10A cells or 4T1 cells were incubated with different concentrations of SPNm or SPNc for 24 h, no obvious cytotoxicity was observed (Fig. S13). Moreover, no obvious hemolysis of erythrocytes was observed after incubation with different concentrations of SPNs for 2 h (Fig. S14). These data suggested the excellent biocompatibility for both nanoparticles. To endow SPNm and SPNc with fluorescent properties for evaluating cellular uptake, boron-dipyrromethene (BODIPY) (4 % w/w) was doped into nanoparticles via nanoprecipitation (Fig. S15) [50]. After treating 4T1 cancer cells with BODIPY-doped SPNm or SPNc for 4 h, strong and similar fluorescence signals were detected via flow cytometry analysis (Fig. S16). Confocal fluorescence images further verified the similar cellular uptake in the cytoplasm of cells at different time slots (Fig. S17), demonstrating the effective and similar endocytosis of both SPNs in 4T1 cancer cells, probably because of their similar sizes and PEG segments.

The in vitro centimeter-scale deep tissue photothermal therapeutic capability of SPNm was studied against 4T1 cancer cells. To mimic the deep tissue environment, a piece of chicken breast tissue with 1 cm thickness was placed on the well plates during NIR-II photoirradiation (Fig. 3a). After treating cells with nanoparticles for 2 h, the cells were first exposed to photoirradiation for 10 min to trigger the release of IOX-1. The photoirradiation was carefully controlled to ensure that the temperature of cancer cells was below 43 °C to minimize photothermal-induced cell death. Subsequently,

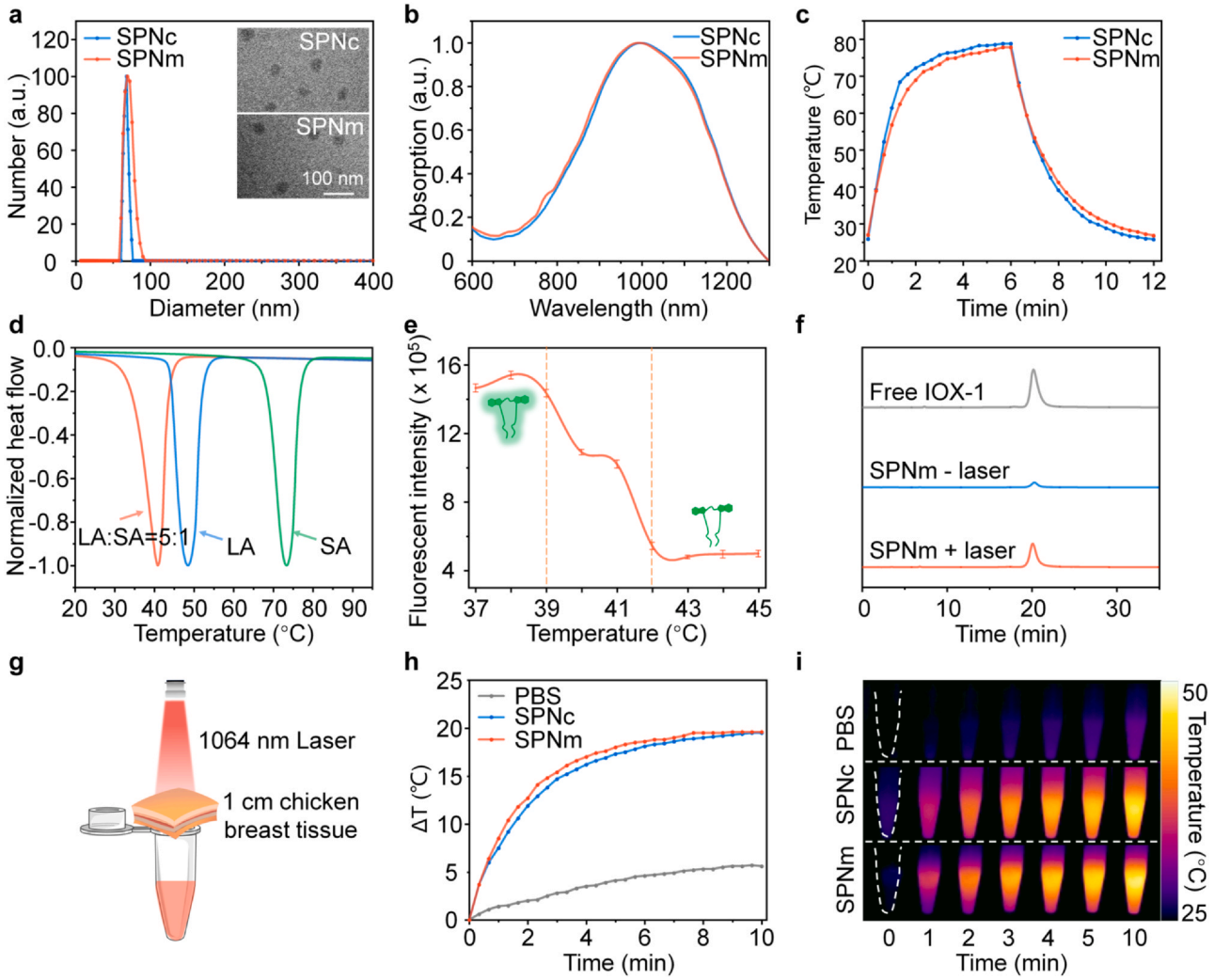

Fig. 2. In vitro characterization of SPNc and SPNm. a) DLS data and TEM images (inset) of SPNc and SPNm. b) Absorption spectra of SPNc and SPNm in water. c) Photothermal properties of SPNc and SPNm by photothermal heating and cooling at a SP concentration of 10 μg mL^{-1} (1064 nm, 1 W cm^{-2}). d) DSC curves of SA and LA at different mass ratios. e) Fluorescence intensity of SPND at 501 nm after incubation at different temperatures for 5 min (n = 3). f) HPLC analysis of IOX-1 released from SPNm with or without 1064 nm laser irradiation (T ≈ 43 °C, 10 min). g) Schematic representation of the centimeter-scale deep tissue photothermal study. h) Temperature change of PBS, SPNc or SPNm (100 μL, the concentration of SP =50 μg mL^{-1}) as a function of laser irradiation time (1064 nm, 1 W cm^{-2}). i) IR thermal images of PBS, SPNc and SPNm at 0, 1, 2, 3, 4, 5 and 10 min under laser irradiation.

the cells were exposed to another NIR-II photoirradiation with a power density of 1 W cm^{-2} after another 2 h of incubation for centimeter-scale deep tissue PTT (Fig. 3a). To evaluate the deep tissue PTT efficacy of these nanoparticles, 4T1 cells were stained with calcein-AM (green fluorescence, viable cells) and propidium iodide (PI) (red fluorescence, dead cells) to detect viable and dead cells through immunofluorescence staining. Obvious red fluorescence signals were detected in SPNm-incubated 4T1 cells after two-step photoirradiation treatment, while almost negligible red fluorescence but strong green fluorescence signals were detected in SPNc-treated cells with the same treatment (Fig. S18). Afterward, the cell viability was quantitatively examined by methyl thiazolyl tetrazolium (MTT) assay. With two-step NIR-II photoirradiation, SPNc-mediated phototherapy caused slight cytotoxicity (cell viability of 77.9 %) to 4T1 cells compared with the PBS group due to the thermotolerance response of cancer cells. In contrast, the cell viability of SPNm-incubated cells decreased to ~45.1 %, which was 2.1-fold lower than that for SPNc-incubated cells (Fig. 3b). These data confirmed that SPNm possesses good photothermal therapeutic ability at centimeter-scale tissue depths.

To investigate the underlying molecular mechanism of SPNm-mediated two-step phototherapy, the expression levels of methylated histone H3K9me2 and HSP90, as the hallmark of the thermotolerance response [50,55], were studied in nanoparticle-treated 4T1 cells by quantitative western blotting analysis and qualitative immunofluorescent staining (Fig. 3c-j and Fig. S19, S20). After two-step NIR-II photoirradiation, SPNm induced substantial upregulation of H3K9me2 in the nucleus of 4T1 cells, which was 2.5-fold higher than the photoirradiation control (SPNc) (Fig. 3c-d, 3i and Fig. S16). Subsequently, the upregulation of H3K9me2 induced by SPNm downregulated the expression of HSP90 in the cytoplasm of 4T1 cells compared to the SPNc group (Figs. 3c, 3e, 3i and Fig. S19). The metastasis inhibition capability of SPNm was further investigated by measuring the expression levels of cancer cell metastasis-related proteins, including c-Jun and MMP-9, after different treatments. The intracellular expression of c-Jun and MMP-9 significantly decreased after treatment with SPNm plus two-step NIR-II photoirradiation, but remained nearly the same for the other treatments (Figs. 3f-h, j and Fig. S20). Thus, these results suggested that IOX-1 was effectively released from SPNm upon NIR-II photoirradiation to inhibit the demethylation function of KDM3A to upregulate the level of

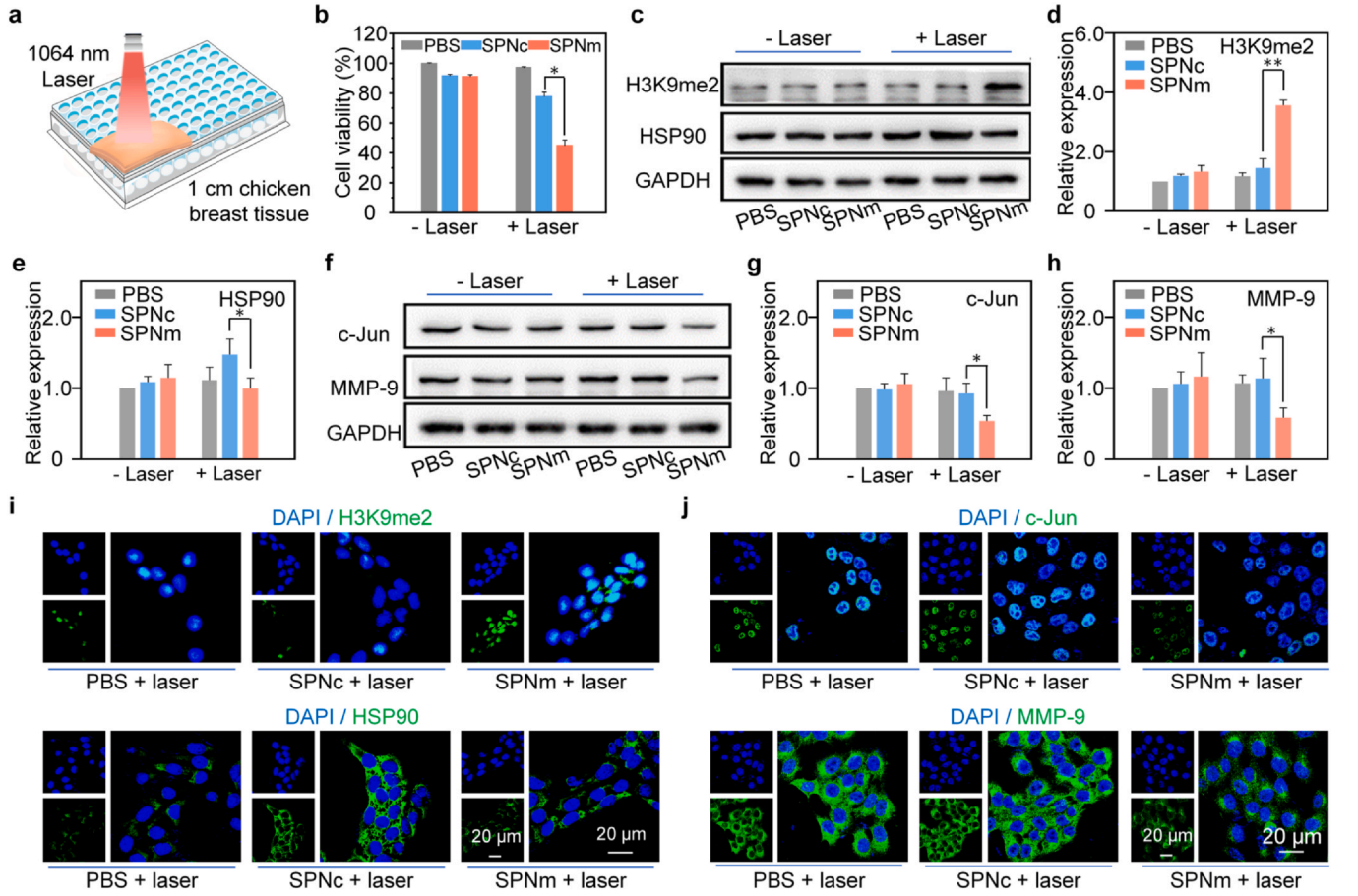

Fig. 3. In vitro SPNm-mediated synergistic cancer therapy and mechanism study. a) Schematic representation of centimeter-scale deep tissue NIR-II phototherapy on cells. The 4T1 cancer cells were treated with PBS, SPNc or SPNm with or without 1064 nm laser irradiation (1.0 W cm^{-2}, 15 min). The concentration of SP = 50 μg mL^{-1}. b) Cell viability of 4T1 cancer cells after different treatments. (n = 3). c) Western blotting analysis of H3K9me2 and HSP90 levels in 4T1 cancer cells after different treatments, with GAPDH as an internal reference. d, e) Quantitative analysis of the d) H3K9me2 and e) HSP90 levels in c (n = 3). f) Western blotting analysis of c-Jun and MMP-9 expression levels in 4T1 cancer cells after different treatments, with GAPDH as an internal reference. g, h) Quantitative analysis of the g) c-Jun and h) MMP-9 expression levels in f (n = 3). i) Confocal fluorescence images of H3K9me2 and HSP90 levels in 4T1 cancer cells with 1064 nm laser irradiation. j) Confocal fluorescence images of c-Jun and MMP-9 expression levels in 4T1 cancer cells with 1064 nm laser irradiation.

H3K9me2, simultaneously resulting in the downregulation of the expression of HSP90 and metastasis-related proteins (c-Jun and MMP-9) for thermal sensitization and metastasis-inhibited synergistic effects against 4T1 cancer cells.

In Vivo SPNm-mediated thermal sensitization and metastasis-inhibited synergistic cancer therapy

SPNm-mediated thermal sensitization and metastasis-inhibited synergistic cancer therapy was further studied in subcutaneous 4T1 tumor-bearing mice. After systemic administration of nanoparticles into mice via the tail vein, the tumors covered by a piece of chicken breast tissue with 1 cm thickness were treated with two-step local NIR-II photoirradiation. After different treatments, the growth of tumors was monitored, and lung metastasis of treated mice was evaluated in the long term (Fig. 4a). To confirm the optimal therapeutic window for NIR-II photoirradiation, both SPNm and SPNc were doped with the NIR fluorogenic dye, silicon 2,3-naphthalocyanine bis(trihexylsilyloxide) (NCBS) (4 % w/w), to form SPNm-NCBS and SPNc-NCBS (Fig. S21 and S22). Thus, the biodistribution of nanoparticles was evaluated by NIR fluorescence imaging. After intravenous injection of SPNm-NCBS or SPNc-NCBS, the fluorescence signals in tumor regions of these groups gradually increased and reached a plateau from 8 to 32 h post-injection time with similar fluorescent intensity (Fig. 4b and c), suggesting the effective accumulation of both nanoparticles into tumors due to their similar hydrodynamic sizes (~70 nm) and PEGylated surfaces. Such a prolonged retention time of SPNm in tumor regions offered a sufficient therapeutic time window for two-step NIR-II photoirradiation. Ex vivo biodistribution results of nanoparticles at 32 h post-injection showed major accumulation in the liver, spleen, and tumor, followed by the lung and other organs (Fig. S23).

Two-step photoirradiation of a centimeter-scale deep-seated tumor was then conducted with a piece of chicken breast tissue with 1 cm thickness covering the tumor to mimic the deep-seated environment. The first NIR-II photoirradiation was applied to the tumors at t = 12 h post-injection of nanoparticles via the tail vein to trigger the release of IOX-1. At this time point, strong green fluorescence signals assigned to SPNs were detected in the cytoplasm of tumor tissues, confirming the effective internalization of both nanoparticles by tumor cells (Fig. S24). The photoirradiation was carefully controlled to ensure that the tumor temperature was below 43 °C to minimize the photothermal effect on tumors. Subsequently, second NIR-II photoirradiation at a power intensity of 1 W cm^{-2} was performed at 24 h post-injection to examine the therapeutic efficiency of SPNm-mediated NIR-II phototherapy of centimeter-scale deep-seated tumors. During the secondary NIR-II photoirradiation, the temperatures of the tumors for SPNm- and SPNc-treated mice gradually increased and similarly reached approximately 46 °C after photoirradiation for 8–14 min (Fig. 4d). After two-step treatments,

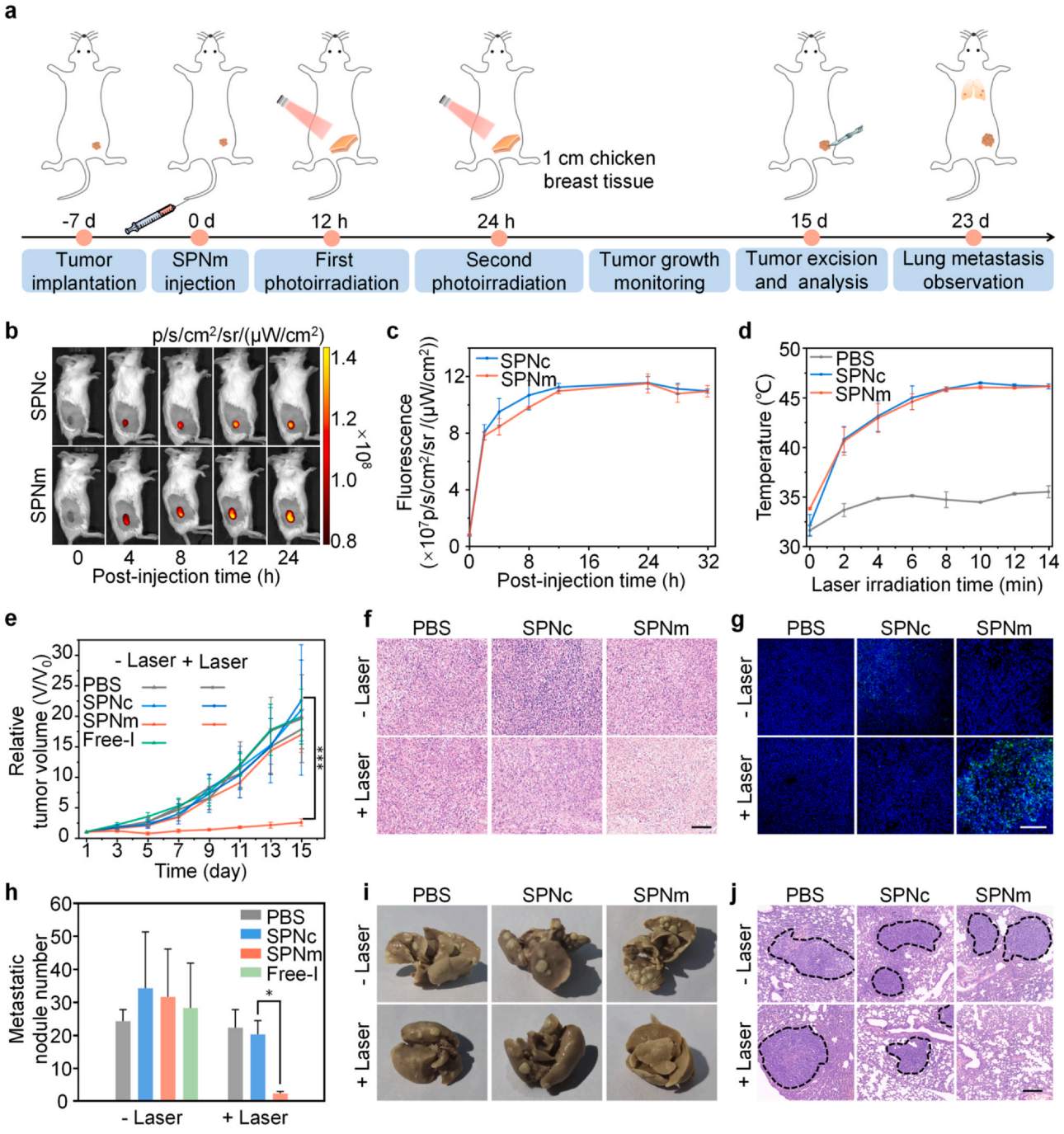

Fig. 4. In vivo SPNm-mediated thermal sensitization and metastasis-inhibited synergistic cancer therapy. a) Schematic of the time schedule for SPNm-mediated thermal sensitization and metastasis-inhibited synergistic cancer therapy. A piece of chicken breast tissue with 1 cm thickness was used to cover the tumor during photoirradiation (1064 nm, 1 W cm^{-2}, 14 min). b) Fluorescence images and c) fluorescence intensity of 4T1 tumor-bearing mice at 0, 2, 4, 8, 12, 24, 28 and 32 h after intravenous injection with NCBS doped SPNc or SPNm (400 μL, the concentration of SP =500 μg mL^{-1}) (n = 2). d) Mean tumor temperature of 4T1 tumor-bearing mice during photoirradiation at 24 h after intravenous injection of PBS, SPNc or SPNm (n = 3). e) Tumor growth curves after treatment with PBS, SPNc, SPNm or free IOX-1 with or without laser irradiation (n = 6). f) H&E staining of tumors after different treatments for 15 days. Scale bars, 100 μm. g) Immunofluorescence caspase-3 staining of tumors after different treatments for 15 days. Green fluorescence indicated caspase-3 staining, while blue fluorescence indicated nuclear staining. Scale bars, 100 μm. h) Number of metastatic nodules per lung after different treatments for 23 days (n = 3). i) Images of metastatic nodules in the lungs after different treatments for 23 days. j) H&E staining of metastatic nodules in the lungs after different treatments for 23 days. Scale bars, 200 μm.

tumor growth curves and lung metastasis of mice were monitored over time. Without photoirradiation, the growth of tumors in SPNm- and SPNc-treated mice was similar to that in PBS-treated mice (Fig. 4e), indicating a negligible therapeutic effect for both SPNs. With photoirradiation, the growth of tumors was not efficiently inhibited in SPNc-treated mice, which demonstrated that such a therapeutic temperature failed to eradicate the tumor cells. In contrast, the tumors in the SPNm-treated mice were nearly completely suppressed. Such an enhanced therapeutic efficacy of SPNm over SPNc was due to the synergistic action of NIR-II PTT and photomanipulation of protein expression. Hematoxylin and eosin (H&E) staining and immunofluorescent staining showed that significant nuclear dissociation of necrotic cells and strong green fluorescence signals (caspase-3) from apoptotic cells were clearly observed in

tumors on SPNm-treated mice after photoirradiation (Figs. 4f, 4g and Fig. S25, S26), while no obvious cell death was detected in the tumors of the other treatment groups.

The metastasis inhibition effect of SPNm-mediated synergistic cancer therapy was investigated by evaluating the metastatic nodules in the lung after 23 days of different treatments (Fig. 4h-j and Fig. S27, S28). No noticeable pulmonary metastatic nodules were observed on SPNm-treated mice after photoirradiation, indicating that SPNm-mediated therapy could effectively inhibit the metastasis of tumors. In contrast, obvious metastatic nodules were detected in the lungs of the mice from the other groups. Furthermore, the body weights of the mice were steady after different treatments (Fig. S29), and no significant histological abnormalities were found in the major organs (Fig. S30). The serum levels of liver/kidney function indicators were normal in healthy mice after treatment with SPNm or SPNc for 14 days (Fig. S31). These results indicated the good biocompatibility of SPNm. Together, these data emphasized that SPNm-mediated synergistic cancer therapy not only suppressed the growth of centimeter-scale deep-seated tumors but also inhibited tumor metastasis to the lung, which was unachievable for other treatments.

In vivo action mechanism of thermal sensitization and metastasis-inhibited synergistic cancer therapy

The underlying molecular mechanism of SPNm-mediated synergistic cancer therapy was investigated. Western blotting analysis indicated significantly upregulated H3K9me2 level after SPNm treatment plus photoirradiation, which was 1.7-fold higher than that in the SPNc injection and photoirradiation treatment group (Fig. 5a and b). The expression levels of HSP90, as the hallmark of the thermotolerance response, were then examined. As expected, compared to the SPNc-treated group, the most significant drop in HSP90 expression was observed in the SPNm-treated group, indicating that SPNm-mediated therapy effectively inhibited the thermotolerance response of cancer cells (Fig. 5a and c). Furthermore, the expression levels of proteins associated with metastasis, including c-Jun and MMP-9, were analyzed by western blotting after various treatments (Fig. 5d-f). c-Jun, a member of activator protein (AP)− 1, regulates cell invasion by upregulating the gene expression required for invasion [56,57]. MMP-9 is a significant protease that promotes metastasis through the breakdown of the physical barrier of the extracellular matrix (ECM) [58–60]. The SPNm-treated group dramatically reduced the expression of c-Jun (to 52.1 %) and MMP-9 (to 72.5 %) compared to the SPNc group (Fig. 5e and f). Consistently, immunofluorescence staining analysis further verified that SPNm-mediated therapy induced enhanced methylated histone H3K9me2 levels and reduced the expression of HSP90 and these metastasis-related proteins (Fig. 5g, h and Fig. S32, S33). According to these results, the molecular mechanism of SPNm-mediated synergistic cancer therapy is summarized in Fig. 5i. The photothermal effect of SPNm released IOX-1, which upregulated the level of H3K9me2 and thus simultaneously impeded the thermotolerance response of cancer cells and downregulated the expression of metastasis-related proteins in tumors at the cellular level, eventually leading to the efficient inhibition of centimeter-scale deep-seated tumors and lung metastasis.

Reduced side effects of SPNm-mediated synergistic cancer therapy

Beyond such superior centimeter-scale deep-seated tumor regression and lung metastasis inhibition performance, SPNm-mediated synergistic cancer therapy could also minimize hyperthermia-induced side effects, including the inflammatory response [61,62] and skin damage [63–65]. In this regard, an orthotopic 4T1 breast tumor model was established in BALB/c mice and mice were subsequently treated with SPNm upon two-step photoirradiation and compared to regular SPNc-treated NIR-II PTT (Fig. 6a). NIR-II PTT was conducted by photoirradiation of the tumors 24 h post-injection of nanoparticles. Notably, the laser power intensity irradiated on the SPNc-treated tumors was set to 1 W cm^{-2}, while that irradiated on the SPNm-treated tumors was set to 0.6 W cm^{-2}. Therefore, the tumor temperature in the SPNc-treated group gradually increased and reached approximately 61 °C after photoirradiation for 6 min, while the tumor temperature in the SPNm-treated group remained at approximately 46 °C (Fig. 6b and c). As expected, both SPNc- and SPNm-treated tumor slides exhibited high expression of caspase-3 and extensive nuclear dissociation (Fig. 6d), indicating significant tumor cell apoptosis and a large necrotic area elicited after SPNc or SPNm treatment. However, the levels of proinflammatory cytokines, including tumor necrosis factor α (TNF-α) and interleukin 6 (IL-6), were significantly elevated in the serum of SPNc-treated and photo-irradiated mice, which were 2.5- (TNF-α levels) and 2.8- (IL-6 levels) folds, respectively, higher than those in the sera of SPNm-treated and photo-irradiated mice (Fig. 6e and f).

In line with the results of proinflammatory cytokine levels in sera, the immunohistochemical (IHC) staining results further confirmed that the levels of TNF-α and IL-6 were significantly increased in tumor tissues of SPNc-treated and photo-irradiated mice, whereas almost no obvious changes in the levels of cytokines were observed after SPNm treatment (Fig. 6g). Furthermore, the reduced side effects of SPNm-mediated therapy were confirmed by H&E staining of the skin-connected therapeutic regions (Fig. 6h). An obvious incomplete epidermal layer and a damaged connective layer above the fatty connective tissue of the hypodermis were found in SPNc-treated and photo-irradiated mice, while it had no significant effects on the skin surface after SPNm treatment. These findings verified that SPNm-mediated synergistic cancer therapy can effectively avoid hyperthermia-induced side effects, including the inflammatory response and skin damage.

Conclusions

Manipulation of intracellular protein expression reliant on heat generated by photothermal agents offers a noninvasive approach to remote control of biological processes. In addition to manipulation of intracellular protein expression, the major function of photothermal agents is local thermal ablation of tumors. In particular, the deeper tissue penetration depth of NIR-II relative to NIR-I light shows the potential of NIR-II PTT for deep-seated cancer treatment [28]. Despite the growing promise in NIR-II PTT, insufficient photothermal ablation in deep-seated tumors limits its clinical applications. The reported record of photothermal ablation depth was restricted to 4 mm through intravenous injection of 2D niobium carbide [66], or 5 mm via intratumoral injection of SPN [67], which was far less than the penetration radius of NIR-II light (at centimeter-scale depth) in biological tissues [68]. This is due to the intrinsic cancer cell thermotolerance mechanism that protects cancer cells from thermal ablation [69]. We herein synthesized an NIR-II photothermal semiconducting polymer nanomanipulator (SPNm) that specifically manipulates the function of the upstream protein KDM3A, which in turn inhibits the expression of KDM3A downstream effector proteins, including the thermotolerance protein HSP90 and metastasis-related proteins of tumor cells, thereby rendering them sensitive to heat, ultimately achieving efficient tumor photothermal ablation at an unprecedented centimeter-scale depth (1 cm) and lung metastasis inhibition. Such superior photothermal ablation depth and metastasis inhibition were attributed to the synergistic action of the NIR-II photothermal therapeutic function and precise photo-manipulation of the protein expression process.

In this synergistic therapeutic system, IOX-1 plays a vital role in upregulating the level of H3K9me2 which in turn simultaneously

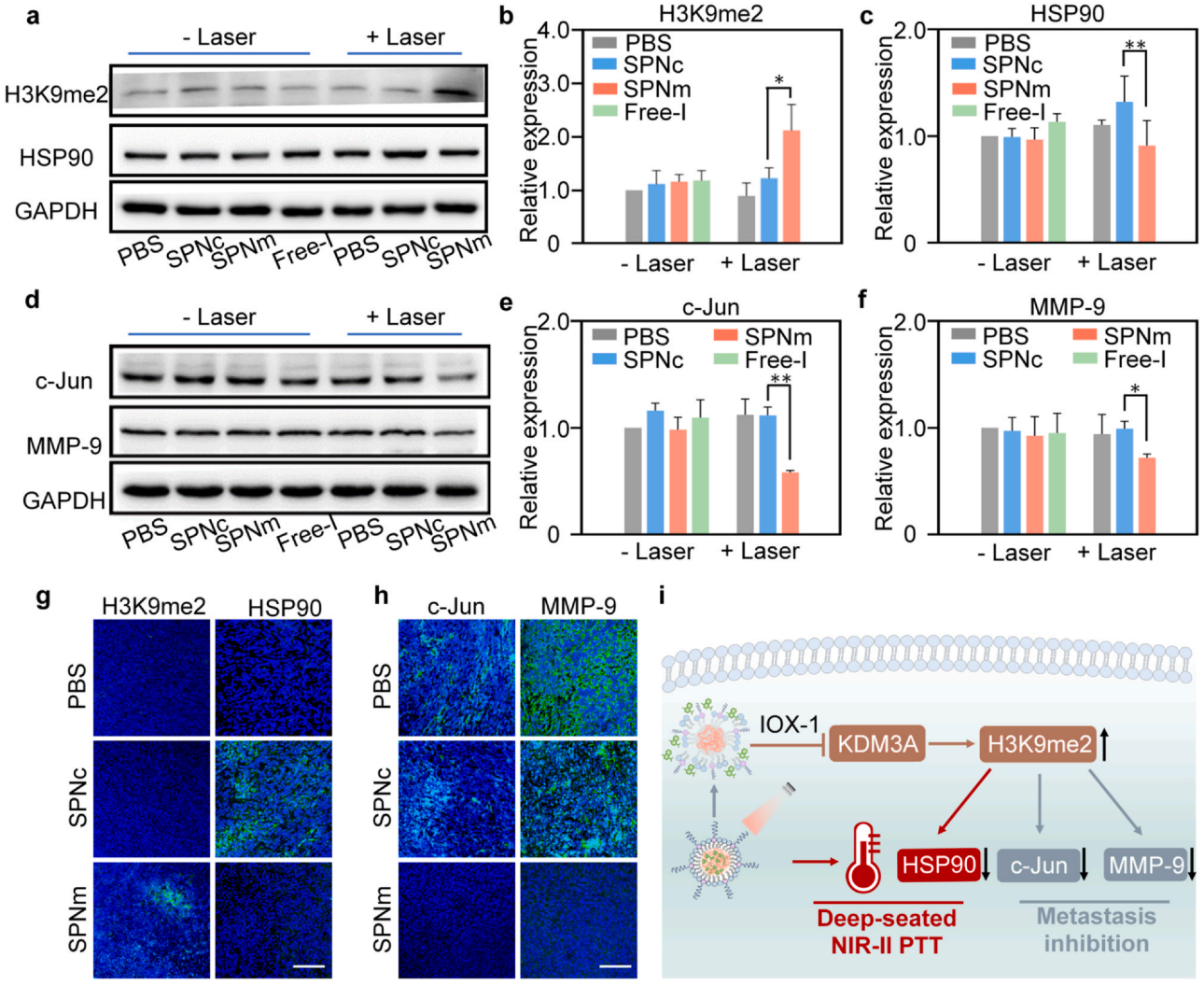

Fig. 5. In vivo action mechanism of SPNm-mediated thermal sensitization and metastasis-inhibited synergistic cancer therapy. a) Western blot images of H3K9me2 and HSP90 levels in tumors at 24 h after different treatments, with GAPDH as an internal reference. b, c) Quantitative analysis of the b) H3K9me2 and c) HSP90 levels in c (n = 3). d) Western blot images of c-Jun and MMP-9 expression levels in tumors for 23 days after different treatments, with GAPDH as an internal reference. e, f) Quantitative analysis of the e) c-Jun and f) MMP-9 expression levels in d (n = 3). g) Confocal fluorescence images of H3K9me2 and HSP90 levels in tumors at 24 h after treatment with PBS, SPNc or SPNm with 1064 nm laser irradiation. h) Confocal fluorescence images of c-Jun and MMP-9 expression levels in tumors for 23 days after treatment with PBS, SPNc or SPNm with 1064 nm laser irradiation. i) Illustration of the molecular mechanism of SPNm-mediated thermal sensitization and metastasis-inhibited synergistic cancer therapy.

downregulates the expression of HSP90 and metastasis-related proteins. However, intravenous injection of free IOX-1 showed limited therapeutic efficacy in tumor-bearing mice (Fig. 4e). This is reasonable because free IOX-1 has poor water solubility and thus cannot effectively accumulate in the tumor region in a small molecular pattern, which indicates the significance of encapsulation of IOX-1 into nanoparticles for cancer therapy. The protein expression changes in tumor-bearing mice after SPNm treatment without photoirradiation were almost negligible. This is because histones are localized in the nucleus but SPNm are localized in the cytoplasm of cancer cells (Fig. 2g and Fig. S14), which demonstrates the necessity of remote-controlled release of IOX-1 via photothermal effects in this therapeutic approach. Moreover, HSP90 inhibitors such as geldanamycin (GA) have been utilized in combination with photothermal agents for mild-temperature photothermal therapy [10,70], and GA-encapsulated SPN (SPNG) also showed a considerable antitumor effect on centimeter-scale deep-seated tumors through our two-step phototherapy strategy (Fig. S34), while the ineffectiveness of SPNG-mediated two-step phototherapy in metastasis inhibition proved the significance of the photo-manipulation upstream protein expression approach for cancer therapy (Fig. S35). In addition, SPNm-mediated synergistic cancer therapy effectively minimized the regular PTT-induced side effects, including the inflammatory response and skin damage (Fig. 6).

In summary, we reported an NIR-II photothermal semiconducting polymer nanomanipulator that integrates photothermal therapeutic function and specific protein expression manipulation ability for thermal sensitization and metastasis-inhibited synergistic cancer therapy. This work not only introduces a promising approach to the remote manipulation of the protein expression process of cancer cells to reinforce antitumor efficacy but also pushes the NIR-II photothermal ablation depth to an unprecedented level. In addition to protein expression manipulators, this strategy can be generalized to develop other thermally controlled therapeutic nanoagents simply by integrating relevant therapeutic molecules into SPNs for enhanced synergistic cancer therapy.

CrediT authorship contribution statement

Min Wu: Methodology, Formal analysis, Investigation, Visualization, Writing – original draft. **Rui Qu:** Formal analysis, Investigation. **Haoze Li:** Formal analysis, Investigation. **Linrong**

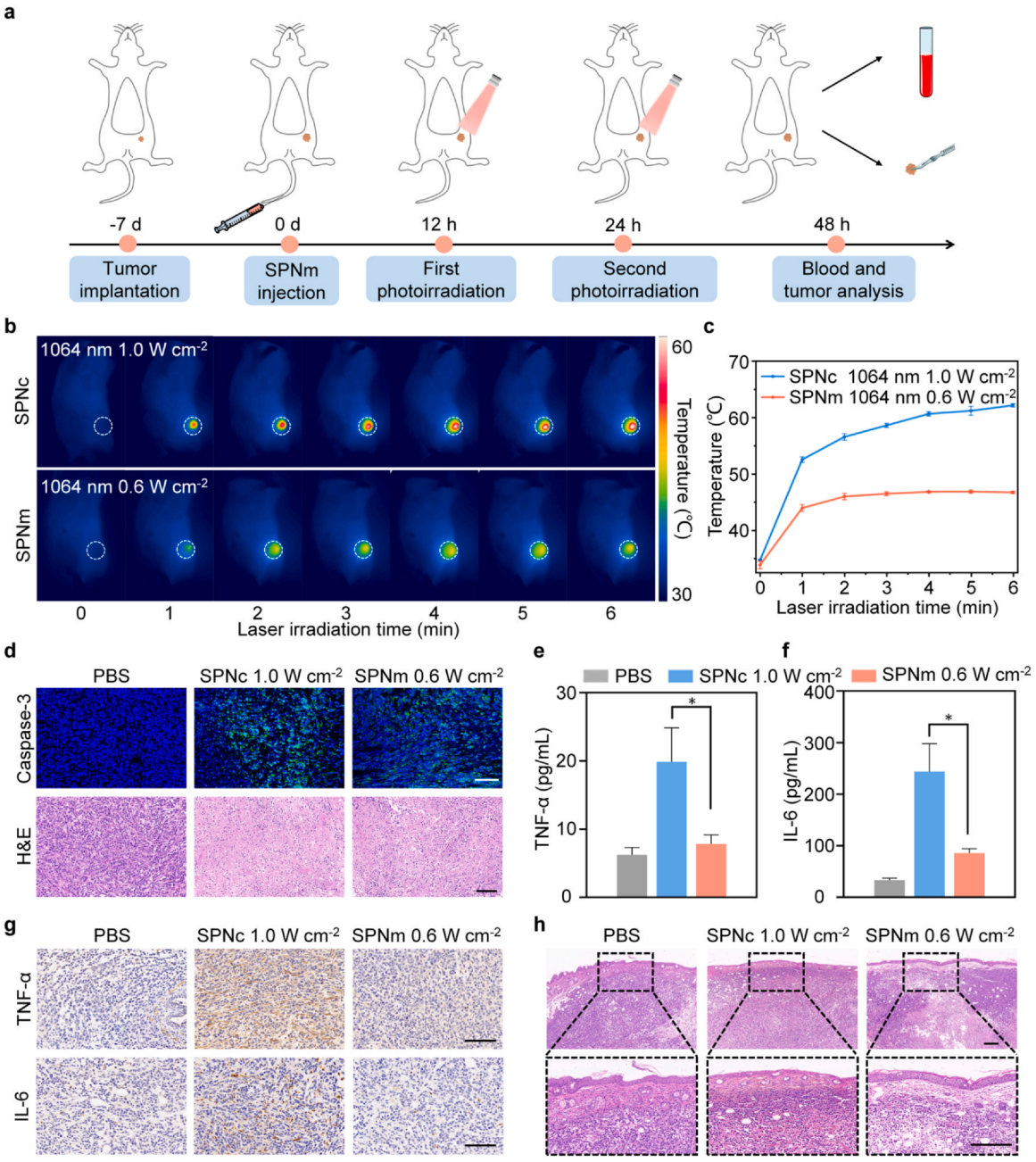

Fig. 6. Reduced side effects of SPNm-mediated synergistic cancer therapy. a) Time schedule of SPNm-mediated synergistic cancer therapy and side effects study. b) IR thermal images of orthotopic 4T1 tumor-bearing mice during photoirradiation (1064 nm) at 24 h post- injection of SPNc or SPNm (200 μL, the concentration of SP =200 μg mL^{-1}, n = 3) for 6 min. Laser conditions: 1 W cm^{-2} for SPNc while 0.6 W cm^{-2} for SPNm. c) Mean tumor temperature during photoirradiation at 24 h post-injection of SPNc or SPNm (n = 3). d) Immunofluorescent caspase-3 staining and H&E staining of tumors after different treatments. Scale bars, 100 μm. e, f) Cytokine levels of e) TNF-α and f) IL-6 in the serum of mice after different treatments (n = 3). g) Immunohistochemical staining analysis of TNF-α and IL-6 in tumor tissues of mice after different treatments. Scale bars, 100 μm. h) H&E staining of the skin-connected therapeutic regions after different treatments. Scale bar = 200 μm.

Chen: Formal analysis, Investigation. **Xiaoke Zhang:** Methodology, Investigation. **Yang Yuan:** Methodology, Investigation. **Weizhi Chen:** Investigation. **Xiqun Jiang:** Conceptualization, Project administration, Resources, Supervision, Writing – review & editing, Funding acquisition. **Xu Zhen:** Conceptualization, Project administration, Resources, Supervision, Writing – review & editing, Funding acquisition.

Data Availability

Data will be made available on request.

Declaration of Competing Interest

The authors declare that they have no known competing financial interests or personal relationships that could have appeared to influence the work reported in this paper.

Acknowledgments

X.Z. and X.J. thank the National Key Research and Development Program of China (No. 2017YFA0701301), National Natural Science Foundation of China (No. 92163214, 21720102005, 51903120, 52173130), and Natural Science Foundation of Jiangsu Province (No.

BK20202002). State Key Laboratory of Analytical Chemistry for Life Science (No. SKLACLS2212) and the Fundamental Research Funds for the Central Universities (No. 020514380274) for financial support.

Appendix A. Supporting information

Supplementary data associated with this article can be found in the online version at doi:10.1016/j.nantod.2022.101691.

References

[1] D. Zhang, G. Wang, X. Yu, T. Wei, L. Farbiak, L.T. Johnson, A.M. Taylor, J. Xu, Y. Hong, H. Zhu, Nat. Nanotechnol. 17 (2022) 777–787.
[2] S.T. Diepstraten, M.A. Anderson, P.E. Czabotar, G. Lessene, A. Strasser, G.L. Kelly, Nat. Rev. Cancer 22 (2022) 45–64.
[3] B. Dale, M. Cheng, K.-S. Park, H.Ü. Kaniskan, Y. Xiong, J. Jin, Nat. Rev. Cancer 21 (2021) 638–654.
[4] J. Liu, Z. Zhao, N. Qiu, Q. Zhou, G. Wang, H. Jiang, Y. Piao, Z. Zhou, J. Tang, Y. Shen, Nat. Commun. 12 (2021) 2425.
[5] A.M. Vargason, A.C. Anselmo, S. Mitragotri, Nat. Biomed. Eng. 5 (2021) 951–967.
[6] T. Narita, S. Yin, C.F. Gelin, C.S. Moreno, M. Yepes, K.C. Nicolaou, E.G. Van, Meir, Clin. Cancer Res. 15 (2009) 6128–6136.
[7] S.H. Li, D.H. Shin, Y.-S. Chun, M.K. Lee, M.-S. Kim, J.-W. Park, Mol. Cancer Ther. 7 (2008) 3729–3738.
[8] R. Napolitano, S. De Matteis, S. Carloni, S. Bruno, G. Abbati, L. Capelli, M. Ghetti, M.T. Bochicchio, C. Liverani, L. Mercatali, Oncol. Rep. 44 (2020) 1561–1573.
[9] T.A. Baudino, Curr. Drug Discov. Technol. 12 (2015) 3–20.
[10] Y. Yang, W. Zhu, Z. Dong, Y. Chao, L. Xu, M. Chen, Z. Liu, Adv. Mater. 29 (2017) 1703588.
[11] X. Zhen, K. Pu, Nano Res. 11 (2018) 5258–5280.
[12] C. Zhang, Z. Zeng, D. Cui, S. He, Y. Jiang, J. Li, J. Huang, K. Pu, Nat. Commun. 12 (2021) 2934.
[13] L. Ge, C. Qiao, Y. Tang, X. Zhang, X. Jiang, Nano Lett. 21 (2021) 3218–3224.
[14] X. Zhen, C. Xie, Y. Jiang, X. Ai, B. Xing, K. Pu, Nano Lett. 18 (2018) 1498–1505.
[15] Y. Li, X. Teng, C. Yang, Y. Wang, L. Wang, Y. Dai, H. Sun, J. Li, Angew. Chem. Int. Ed. 60 (2021) 5083–5090.
[16] L. Tu, Z. Liao, Z. Luo, Y.L. Wu, A. Herrmann, S. Huo, Exploration 1 (2021) 20210023.
[17] Y. Li, M. Jiang, Z. Deng, S. Zeng, J. Hao, Adv. Sci. 8 (2021) 2004391.
[18] J. Li, Y. Luo, K. Pu, Angew. Chem. Int. Ed. 60 (2021) 12682–12705.
[19] R. Xiong, D. Hua, J. Van Hoeck, D. Berdecka, L. Léger, S. De Munter, J.C. Fraire, L. Raes, A. Harizaj, F. Sauvage, Nat. Nanotechnol. 16 (2021) 1281–1291.
[20] H. Sun, Q. Zhang, J. Li, S. Peng, X. Wang, R. Cai, Nano Today 37 (2021) 101073.
[21] M.D. Liu, D.K. Guo, R.Y. Zeng, W.H. Guo, X.L. Ding, C.X. Li, Y. Chen, Y. Sun, X.Z. Zhang, Small Methods 5 (2021) e2100361.
[22] W. Zhou, Y. Zhang, S. Meng, C. Xing, M. Ma, Z. Liu, C. Yang, T. Kong, Small Methods 5 (2021) e2000920.
[23] H. Wang, Z. He, X.-A. Liu, Y. Huang, J. Hou, W. Zhang, D. Ding, Small Struct. 3 (2022) 2200036.
[24] J. Li, C. Xie, J. Huang, Y. Jiang, Q. Miao, K. Pu, Angew. Chem. Int. Ed. 57 (2018) 3995–3998.
[25] Y. Lyu, D. Cui, H. Sun, Y. Miao, H. Duan, K. Pu, Angew. Chem. Int. Ed. 56 (2017) 9155–9159.
[26] H. Chu, J. Zhao, Y. Mi, Z. Di, L. Li, Nat. Commun. 10 (2019) 2839.
[27] X. Zhen, X. Jiang, WIREs Nanomed. Nanobiotechnol. (2019) e1593.
[28] A.M. Smith, M.C. Mancini, S. Nie, Nat. Nanotechnol. 4 (2009) 710–711.
[29] A.S. Schwartz-Duval, C.J. Konopka, P. Moitra, E.A. Daza, I. Srivastava, E.V. Johnson, T.L. Kampert, S. Fayn, A. Haran, L.W. Dobrucki, Nat. Commun. 11 (2020) 4530.
[30] X. Song, W. Zhu, X. Ge, R. Li, S. Li, X. Chen, J. Song, J. Xie, X. Chen, H. Yang, Angew. Chem. Int. Ed. 60 (2021) 1306–1312.
[31] K. Hu, L. Xie, Y. Zhang, M. Hanyu, Z. Yang, K. Nagatsu, H. Suzuki, J. Ouyang, X. Ji, J. Wei, Nat. Commun. 11 (2020) 2778.
[32] B. Ma, A. Bianco, Small 17 (2021) 2102557.
[33] R. Qu, X. Zhen, X. Jiang, CCS Chem. 4 (2022) 401–419.
[34] Y. Qin, X. Chen, Y. Gui, H. Wang, B.Z. Tang, D. Wang, J. Am. Chem. Soc. 144 (2022) 12825–12833.
[35] H.S. Jung, P. Verwilst, A. Sharma, J. Shin, J.L. Sessler, J.S. Kim, Chem. Soc. Rev. 47 (2018) 2280–2297.
[36] K. Wanderi, Z. Cui, Exploration 2 (2022) 20210097.
[37] X. Zhen, C. Zhang, C. Xie, Q. Miao, K.L. Lim, K. Pu, ACS Nano 10 (2016) 6400–6409.
[38] X. Zhen, K. Pu, X. Jiang, Small 17 (2021) 2004723.
[39] J. Li, X. Zhen, Y. Lyu, Y. Jiang, J. Huang, K. Pu, ACS Nano 12 (2018) 8520–8530.
[40] X. Wang, M. Wu, H. Li, J. Jiang, S. Zhou, W. Chen, C. Xie, X. Zhen, X. Jiang, Adv. Sci. 9 (2022) 2104125.
[41] X. Wang, X. Zhen, X. Jiang, Acta Polym. Sin. 52 (2021) 687–707.
[42] X. Zhen, C. Xie, K. Pu, Angew. Chem. Int. Ed. 57 (2018) 3938–3942.
[43] C. Xie, X. Zhen, Q. Miao, Y. Lyu, K. Pu, Adv. Mater. 30 (2018) 1801331.
[44] X. Duan, Q. Zhang, Y. Jiang, X. Wu, X. Yue, Y. Geng, J. Shen, D. Ding, Adv. Mater. 34 (2022) e2200179.
[45] S.P. Rowbotham, F. Li, A.F.M. Dost, S.M. Louie, B.P. Marsh, P. Pessina, C.R. Anbarasu, C.F. Brainson, S.J. Tuminello, A. Lieberman, S. Ryeom, T.M. Schlaeger, B.J. Aronow, H. Watanabe, K.K. Wong, C.F. Kim, Nat. Commun. 9 (2018) 4559.
[46] J. Yoo, Y.H. Jeon, H.Y. Cho, S.W. Lee, G.W. Kim, D.H. Lee, S.H. Kwon, Cancers 12 (2020) 1098.
[47] Y. Jiang, C. Li, Q. Wu, P. An, L. Huang, J. Wang, C. Chen, X. Chen, F. Zhang, L. Ma, Nat. Commun. 10 (2019) 2935.
[48] G. Qing, X. Zhao, N. Gong, J. Chen, X. Li, Y. Gan, Y. Wang, Z. Zhang, Y. Zhang, W. Guo, Y. Luo, X.J. Liang, Nat. Commun. 10 (2019) 4336.
[49] C. Zhu, D. Huo, Q. Chen, J. Xue, S. Shen, Y. Xia, Adv. Mater. 29 (2017) 1703702.
[50] M.B. Cheng, Y. Zhang, C.Y. Cao, W.L. Zhang, Y. Zhang, Y.F. Shen, PLoS Biol. 12 (2014) e1002026.
[51] S. Ramadoss, G. Guo, C.Y. Wang, Oncogene 36 (2017) 47–59.
[52] K. Zhang, I.A. Ahmed, H.T. Kratochvil, W.F. DeGrado, F. Gai, H. Jo, Chem. Comm. 55 (2019) 5095–5098.
[53] E.M. Knavel, C.L. Brace, Tech. Vasc. Interv. Radiol. 16 (2013) 192–200.
[54] B. Hildebrandt, P. Wust, O. Ahlers, A. Dieing, G. Sreenivasa, T. Kerner, R. Felix, H. Riess, Crit. Rev. Oncol. Hematol. 43 (2002) 33–56.
[55] J.K. Das, X. Xiong, X. Ren, J.M. Yang, J. Song, J. Oncol. 2019 (2019) 3267207.
[56] L.M. LaFave, J.D. Buenrostro, Nat. Cancer 2 (2021) 14–15.
[57] A.C. Watt, P. Cejas, M.J. DeCristo, O. Metzger-Filho, E.Y. Lam, X. Qiu, H. BrinJones, N. Kesten, R. Coulson, A. Font-Tello, Nat. Cancer 2 (2021) 34–48.
[58] J. Winkler, A. Abisoye-Ogunniyan, K.J. Metcalf, Z. Werb, Nat. Commun. 11 (2020) 5120.
[59] T.R. Cox, Nat. Rev. Cancer 21 (2021) 217–238.
[60] X. Bi, P. Lou, Y. Song, X. Sheng, R. Liu, M. Deng, X. Yang, G. Li, S. Yuan, H. Zhang, Oncogene 40 (2021) 4832–4845.
[61] M. Li, S. Li, H. Zhou, X. Tang, Y. Wu, W. Jiang, Z. Tian, X. Zhou, X. Yang, Y. Wang, Nat. Commun. 11 (2020) 1126.
[62] Q. Dong, X. Wang, X. Hu, L. Xiao, L. Zhang, L. Song, M. Xu, Y. Zou, L. Chen, Z. Chen, W. Tan, Angew. Chem. Int. Ed. 130 (2018) 183–187.
[63] Y. Liu, X. Zhu, Z. Wei, W. Feng, L. Li, L. Ma, F. Li, J. Zhou, Adv. Mater. 33 (2021) 2008615.
[64] X. Zhu, W. Feng, J. Chang, Y.W. Tan, J. Li, M. Chen, Y. Sun, F. Li, Nat. Commun. 7 (2016) 10437.
[65] J.G. Piao, D. Liu, K. Hu, L. Wang, F. Gao, Y. Xiong, L. Yang, ACS Appl. Mater. Interfaces 8 (2016) 2847–2856.
[66] H. Lin, S. Gao, C. Dai, Y. Chen, J. Shi, J. Am. Chem. Soc. 139 (2017) 16235–16247.
[67] Y. Jiang, J. Li, X. Zhen, C. Xie, K. Pu, Adv. Mater. 30 (2018) 1705980.
[68] C. Ash, M. Dubec, K. Donne, T. Bashford, Lasers Med. Sci. 32 (2017) 1909–1918.
[69] R.I. Morimoto, M.G. Santoro, Nat. Biotechnol. 16 (1998) 833–838.
[70] G. Gao, X. Sun, G. Liang, Adv. Funct. Mater. 31 (2021) 2100738.